Hemodynamics analyses of arterial expansions with implications to thrombosis and restenosis

S. Hyun [a], C. Kleinstreuer [a,*], J.P. Archie Jr [a, b]

[a] *Department of Mechanical and Aerospace Engineering, North Carolina State University, Raleigh, NC 27695-7910, USA*
[b] *Wake Medical Center, Raleigh, NC, USA*

Abstract

It is assumed that critical hemodynamic factors play an important role in the onset, localization and degree of post-operative complications, for example, thrombosis and restenosis. Of special interest are sudden expansion flows, which may occur in straight artery segments such as the common carotid after endarterectomy or end-to-end anastomoses. Sudden expansion geometries are possible origins of early post-operative emboli and significant myointimal hyperplasia resulting in early or late complications. Transient laminar axisymmetric and fully three-dimensional blood flows were simulated employing a validated finite volume code in conjunction with a Runge–Kutta particle tracking technique. Disturbed flow indicators, which may predict the onset of thrombosis and/or restenosis, were identified and employed to evaluate 90°-step and smooth expansion geometries.

Smooth expansion geometries have weaker disturbed flow features than step expansion geometries. Specifically, the regions near the expansion wall and the reattachment point are susceptible to both atherosclerotic lesion and thrombi formations as indicated by non-uniform hemodynamic indicators such as near-zero wall shear stress and elevated wall shear stress gradients as well as blood particle accumulation and deposition. A new parameter, the wall shear stress angle deviation (WSSAD) has been introduced, which indicates areas of abnormal endothelial cell morphology and particle wall deposition. In turn, regions of low wall shear stress and high wall shear stress gradients are recognized as susceptible sites for arterial diseases. Thus, it is interesting to note that high WSSAD surface areas cover low wall shear stress, high wall shear stress gradient locations as well as high wall particle deposition.

A gradual change in step expansion geometry provides better results in terms of WSSAD values and hence potentially reducing atherosclerosis as well as thrombi formation. © 2000 IPEM. Published by Elsevier Science Ltd. All rights reserved.

Keywords: Computational hemodynamics simulations; Transient particle-hemodynamics; Sudden and smooth expansions; Arterial disease indicators; Thrombosis; Restenosis

1. Introduction

Although the actual causes of arterial diseases are multifactorial and not exactly known, it has been suggested that a locally dysfunctional endothelium and the migration of low density lipoproteins and monocytes into the arterial wall indicate the onset of atherosclerosis. Furthermore, activated platelets, fibres and blood cells may form thrombi in disturbed flow regions. Disturbed flow indicators, which include extreme wall shear stresses and their variations, correlate with arterial wall dysfunctions as well as local blood particle accumulation and may lead to renewed atheroma and/or thrombosis [1–8]. Of interest here are sudden expansions as they may occur in a number of arterial geometries, including the proximal regions of straight endarterectomized artery segments, end-to-end anastomoses, and in areas of balloon angioplasty with or without stent placement.

For example, it has been speculated that early post-operative emboli originate at the common carotid step after endarterectomy [9]. Although much attention has been given to managing the internal carotid end point, patch reconstruction, and prevention of early post-operative emboli, no study was found which considers a correlation between the presence of a step and conditions for early post-operative emboli. Archie [9] also postulated that the local potential for mobility due to oscillat-

* Corresponding author. Tel.: +1-919-515-5261; fax: +1-919-515-7968.

E-mail address: ck@eos.ncsu.edu (C. Kleinstreuer).

ing pressures and high wall shear stress gradients in this zone of disturbed flow may promote both dislodgment of components of the exposed intima and media as well as the formation of platelet-fibrin thrombi.

Endothelial cells form a protective barrier and are the mass transfer regulator, covering the blood vessel walls. They tend to align themselves with the flow field and have an elongated tear drop configuration in steady laminar flow. This means that wall shear stress changes may alter the endothelial cells in shape as well as function. According to the studies of Okano and Yoshida [10] and Nerem et al. [11] atherosclerotic lesion-prone regions are covered with irregular round-shaped endothelial cells, with an increased intercellular permeability.

While it is rather difficult to measure transient three-dimensional fluid-particle flow fields, the characteristics of axisymmetric flow fields with particle trajectories in, for example, straight arteries can be readily obtained via direct velocity measurements and visualization techniques [12–17]. Of particular interest are the experimental results of Karino and Goldsmith [15] and Blackshear et al. [17] who showed that a recirculation region is an attractive place for thrombi formation. In addition, Karino et al. [16] and Pritchard et al. [18] showed that particle deposition has a tendency to increase near the reattachment point where higher normal velocities toward the wall exist. Complementary to experimental studies of particle trajectories, computational analyses of arterial particle-hemodynamics may reveal more detailed information [19–25]. For example, Kunov et al. [20] studied particle residence times for an axisymmetric stenosed tube. They introduced the concept of volumetric residence time based on particle motion, accumulation, and residence in a given location. Buchanan and Kleinstreuer [19] analyzed transient particle distributions and monocyte trajectories in a straight tube with a smooth partial occlusion. Kleinstreuer and Hyun [24] showed that the maximum particle wall deposition is located near the reattachment point for steady as well as pulsatile sudden expansion flows using a Lagrangian particle transport model. Their results matched the experimental observations by Karino and Goldsmith [15] and Pritchard et al. [18].

This paper focuses on endarterectomized common carotid arteries with different symmetric and asymmetric expansion geometries, i.e., 90°-step as well as smooth expansions, connecting the partially occluded section upstream and the surgically restored section downstream (cf. Fig. 1b). The majority of proximal endarterectomy end-points in the common carotid artery are eccentric because of the circumferential changes in intimal thickening. Hence, we are focusing mainly on the non-concentric common carotid step. Considering a Casson-type fluid, the transient Lagrangian particle-hemodynamics are simulated for the tubular two- and three-dimensional configurations. Time-averaged wall shear stresses (WSS)

a) Representative input pulse
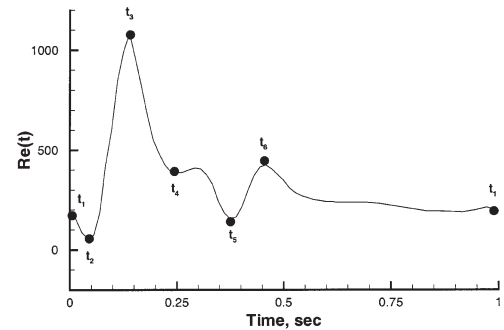
b) Diseased and endarterectomized artery segment
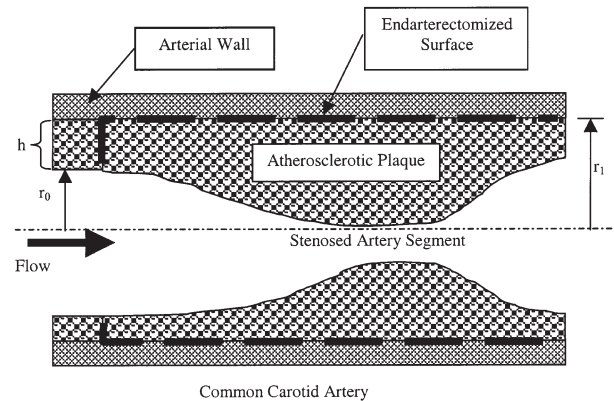
Fig. 1. System schematics: (a) Input pulse for common carotid artery; and (b) Stenosed artery segment.

and their spatial gradients (WSSG) are considered as non-uniform hemodynamic indicators. Due to its strong dependency on the type of input pulse [26], the discussion of the oscillatory shear index (OSI) is excluded in this paper. In addition to calculating the wall shear stress and its gradients, a new indicator, the wall shear stress angle deviation (WSSAD) is introduced and its implications to thrombosis and renewed atheroma are discussed.

2. Theory

2.1. Flow equations

The system geometry with a typical flow input waveform of the common carotid artery are shown in Fig. 1a and b. The input pulse in terms of Reynolds number at the inlet (Fig. 1a) is taken from Bharadvaj et al. [32]. The period of the input pulse is 1 s and Womersley number, which is calculated by $r_o \sqrt{\dfrac{2\pi}{T} \dfrac{1}{v}}$, is about 3.8. The

radius of the inlet tube is 2 mm and a "plaque layer" has been removed downstream inside the common carotid (cf. Fig. 1b), widening the lumen back to its original shape with r_1=4 mm. The remaining plaque upstream is assumed to be uniform with a variable step height of h_{min}=0.5 mm and h_{max}=2 mm [9]. The computational inlet tube length is 30 times r_1 and the outlet tube length is 50 times r_1, which are sufficient to obtain fully developed transient velocity profiles [2].

Considering transient laminar, incompressible flow of a non-Newtonian fluid and rigid arterial walls, the governing equations [27] are continuity:

$$\nabla \cdot \vec{v} = 0 \tag{1}$$

and linear momentum:

$$\frac{\partial \vec{v}}{\partial t} + (\vec{v} \cdot \nabla)\vec{v} = \frac{1}{\rho}(-\nabla p + \nabla \cdot \vec{\vec{\tau}}) \tag{2}$$

The blood rheology is represented by:

$$\vec{\vec{\tau}} = 2\eta(II_D)\vec{\vec{D}} \tag{3}$$

where $\vec{\vec{D}} = \frac{1}{2}[\nabla \vec{v} + (\nabla \vec{v})^T]$ while $\vec{\vec{\gamma}} = 2\vec{\vec{D}}$ and η is a function of the shear rate given by an extended Casson model [28] as:

$$\eta(II_D) = \frac{1}{2\sqrt{II_D}}[C_1(Ht) + C_2(Ht)\sqrt{2\sqrt{II_D}}]^2 \tag{4}$$

where

$$II_D = \frac{1}{2}[(tr\vec{\vec{D}})^2 + tr(\vec{\vec{D}})^2] \tag{5}$$

The coefficients C_1 and C_2 in Eq. (4) were determined for a hematocrit of Ht=40% as C_1 =0.2 (dyn/cm²)^{1/2} and C_2 =0.18 (dyn·s/cm²)^{1/2} based on Merrill's experimental data [29]. The asymptotic value of the viscosity Ht=40% was taken as the Newtonian viscosity μ=0.0348 dyn·s/cm², which guarantees a smooth transition from the Casson model to a Newtonian fluid. Since the Casson model is only suitable for shear rates $\dot{\gamma}>1$ (s⁻¹), we take η =0.1444 dyn.s/cm² when $\dot{\gamma}<1$ (s⁻¹), which is the "zero-shearrate" condition. All the values given are at 37°C.

The auxiliary boundary conditions are a parabolic axial velocity profile at the inlet in form of $Re_d(t)$ (no radial and circumferential velocities), fully developed velocity at the outlet, and no slip condition at the wall. Fig. 2 depicts the finite volume meshes for axisymmetric geometries (Fig. 2a and b) and asymmetric geometries

(Fig. 2c and d) considering 90°-step as well as smooth expansions.

2.2. Blood particle dynamics

To predict the particle motion in pulsatile blood flow, a Lagrangian approach is employed. The trajectory of a particle suspended by the fluid flow is governed by the rate of change of momentum and the external forces acting upon it. The basic assumptions for the particle motion analysis include non-interacting solid spheres as well as negligible pressure gradient force and Basset force. Due to the pulsatility of the blood flow, the particle motion is governed by the drag force and the particle acceleration effect. Thus, in the framework of the Lagrangian formulation, the equation of motion of a representative particle of mass m_p can be written as:

$$\left(m_p + \frac{m_f}{2}\right)\frac{d^2\vec{x}_p}{dt^2} = \vec{F}_d \tag{6}$$

The second term in the parenthesis on the left hand side is the virtual mass term for the accelerating particle, where m_f is the mass of the fluid occupied by the particle. The drag force $\vec{F}_d$ is of the form

$$\vec{F}_d = \frac{1}{8}\pi\rho d_p^2 C_d \vec{w}_r|\vec{w}_r| \tag{7}$$

where ρ is particle density, d_p is particle diameter, $\vec{v}_f$ is fluid velocity where the particle center is, $\vec{v}_p$ is the particle velocity, $\vec{w}_r = \vec{v}_f - \vec{v}_p$ is the relative velocity, and C_d has been obtained from Stokes flow condition

$$C_d = 24/Re_p \tag{8}$$

Here, Re_p is the particle Reynolds number based on the absolute value of the relative velocity, $|\vec{w}_r|$, the diameter of the particle, d_p, and the viscosity of the fluid, v. In this study, a particle represents a monocyte with a diameter of 14 μm and a density of 1.08 g/cc, and it is assumed to be "deposited" when it approaches the wall within one radius, i.e. 7 μm.

2.3. Arterial disease indicators

The local wall shear stress and its variations can be employed as the "disturbed flow" indicators, which identify the regions where potentially an arterial disease process may start. It is assumed that high wall shear stress areas may be sites of endothelial cell dysfunction and platelet activation, leading to blood particle aggregation and possible surface attachment in regions of minimal shear stresses [30], whereas sustained non-zero

a) Mesh for axisymmetric step expansion

b) Mesh for axisymmetric smooth expansion

c) Mesh for asymmetric step expansion

Cross-section mesh for inlet tube

Cross-section mesh for exit tube

d) Mesh for asymmetric smooth expansion

Cross-section mesh for inlet tube

Cross-section mesh for exit tube
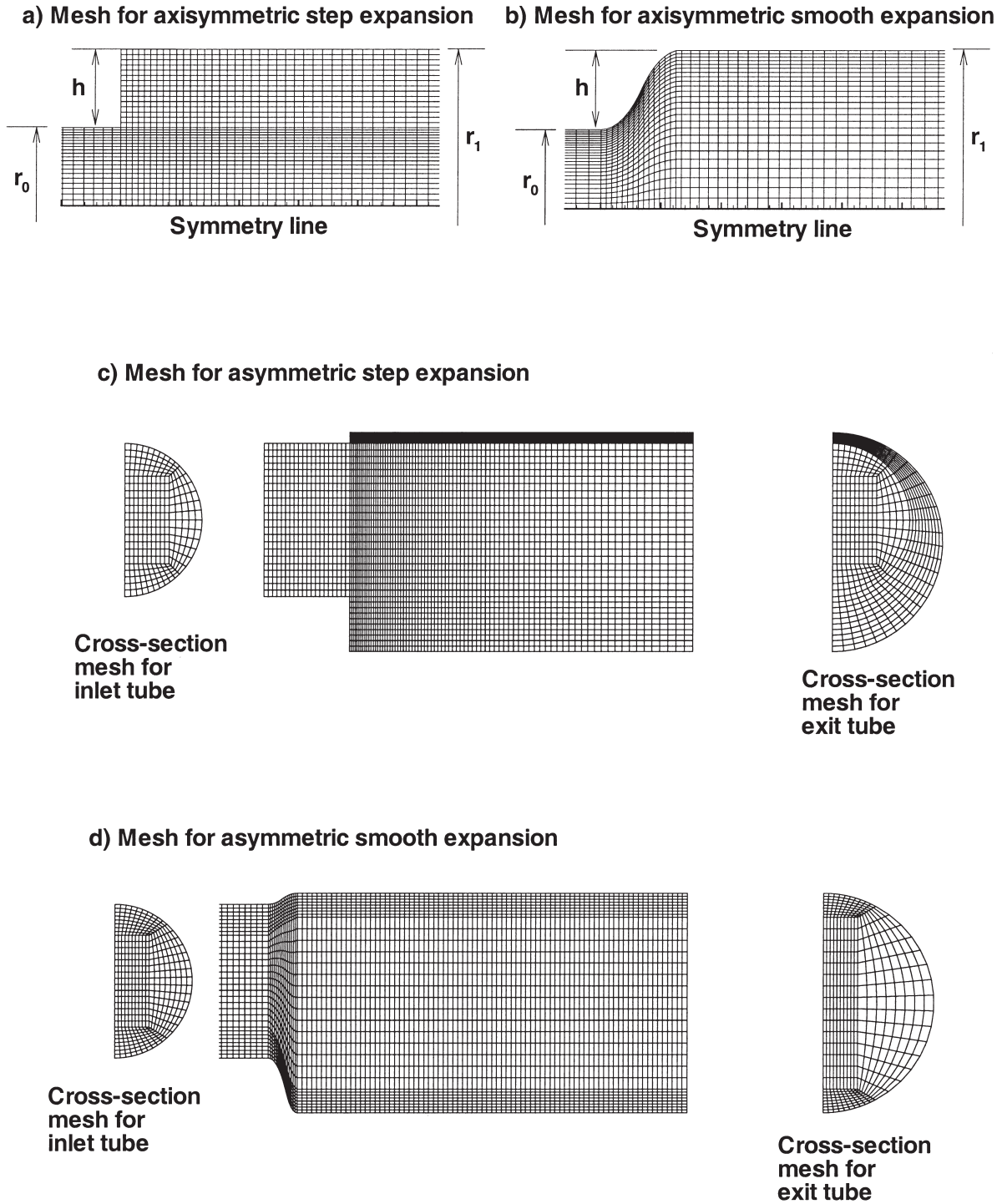
Fig. 2.   Computational meshes for expansion geometries.

wall shear stress gradients are indicators of sites susceptible to restenosis [1,31] The *new* indicator, i.e., the wall shear stress angle deviation (WSSAD), may turn out to be a suitable parameter in the interpretation of physico-biological processes leading to arterial diseases [24].

The six-component stress tensor in Eqs. (2) and (3) reduces to a two-component shear stress vector at the wall, i.e.

$$\vec{\tau} \Rightarrow \vec{\tau}_w = (\tau_{w,m}, \tau_{w,n}) \tag{9a-c}$$

$$\text{or } \tau_w = |\vec{\tau}_w| \text{ and } |\overline{WSS}| = \frac{1}{T}\int_0^T |\vec{\tau}_w| dt$$

The wall shear stress gradient (WSSG) captures the aggravating impact of temporal and spatial *changes* in wall shear on the lumen surface. It was suggested that, when compared to clinical observations, high-sustained WSSG-values could be correlated with susceptible sites of restenosis, i.e., the onset of atherosclerosis and/or hyperplasia [1,31]. Specifically, the time-averaged WSSG is defined as:

$$\overline{|\mathrm{WSSG}|}=\frac{1}{T}\int_0^T |\mathrm{WSSG}|dt \tag{10a}$$

where

$$|\mathrm{WSSG}|=[(\partial \tau_{w,m}/\partial m)^2+(\partial \tau_{w,n}/\partial n)^2]^{1/2} \tag{10b}$$

where T is a period of input pulse, m indicates the mean flow or $\tau_{w,mean}$ direction, and n is the normal to m on the surface. While endothelial cells align themselves with $\tau_{w,mean}$, the instantaneous τ_w may differ.

A new quantitative predictor for the spatial changes of wall shear stress direction links aggravating hemodynamics with abnormal endothelial cell morphology and incorporates the motion of fluid elements or blood particles towards the arterial wall. Regions with round or polygonal endothelial cells, which were affected by the aggravating wall shear stress environment, coincide with areas of elevated endothelium permeability [10,11]. While the flow moves toward the wall, problematic particles (e.g. monocytes) may have a chance to adhere to the endothelium and migrate into the wall at sites of increased permeability. The mathematical expression for the WSSAD in a general coordinate system is computed as the mean angle between $\vec{\tau}_i$ and the surrounding shear stresses ($\vec{\tau}_j$) with normal velocity effect on the particle motion as follows:

$$\mathrm{WSSAD}=C^*\mathrm{arccos}\left(\frac{\overline{\vec{\tau}}_i\cdot\overline{\vec{\tau}}_j}{|\overline{\vec{\tau}}_i|\cdot|\overline{\vec{\tau}}_j|}\right) \tag{12a}$$

where

$$C=\begin{cases}1.0; & \overline{\vec{v}}_{n,i}\cdot\vec{n}_i\geq0 \\ 0.0; & \overline{\vec{v}}_{n,i}\cdot\vec{n}_i<0\end{cases} \tag{12b}$$

and

$$\overline{\vec{\tau}}_i=\frac{1}{T}\int_0^T \vec{\tau}_i dt,\quad \overline{\vec{v}}_i=\frac{1}{T}\int_0^T \vec{v}_n dt \tag{12c-d}$$

Here $\overline{\vec{\tau}}_i$ is the time-averaged wall shear stress vector at surface point i, $\overline{\vec{v}}_{n,i}$ is the time averaged, near-wall velocity component normal to the surface i, $\vec{n}$ is the normal vector of the wall, T is the period of the input pulse, subscript i is for the current node and j is an index for neighboring cells. Typically, with j=1,2,3,4 a mean WSSAD is computed for each location i. The factor C emphasizes the potential impact of approaching flow, i.e., implying possible particle deposition on surface element i; C=0, for example, at flow separation points. In three-dimensional flow fields, WSSAD values vary between 0 and π indicating the least and most severe conditions, respectively.

2.4. Numerical method

The numerical calculations have been carried out with a validated finite volume-based algorithm CFX 4.2 with the SIMPLEC algorithm for the pressure correction and an algebraic multi-grid (AMG) scheme for the speed-up of the inner iterations [32–34]. Lei [31], and Hyun [35] have documented details of in-house numerical program improvements and extensions for calculations of the disturbed flow indicators and the transient particle transport.

In this study, a body-fitted coordinate system for the computational domain has been used (cf. Fig. 2a-d). The height (h) of expansion is assumed 2 mm for axisymmetric geometries (cf. Fig. 2a and b). For the asymmetric geometries, a variable step height of 0.5 mm for a smaller expansion and h_{max}=2 mm for a larger one is applied and inlet and exit tubes are connected eccentri-
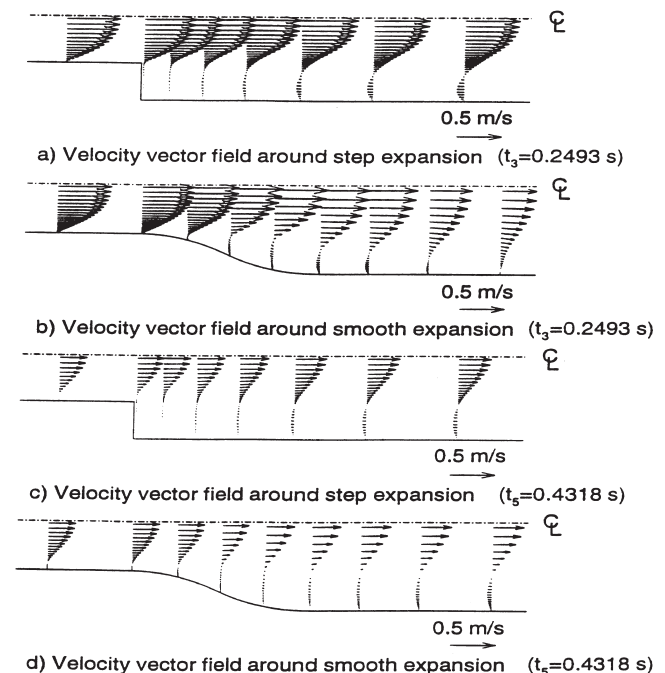
Fig. 3. Velocity vector fields for axisymmetric expansion geometries at representative time steps.

a) Velocity vector field for symmetry plane (t₃)

d) Velocity vector field for symmetric plane (t₅)
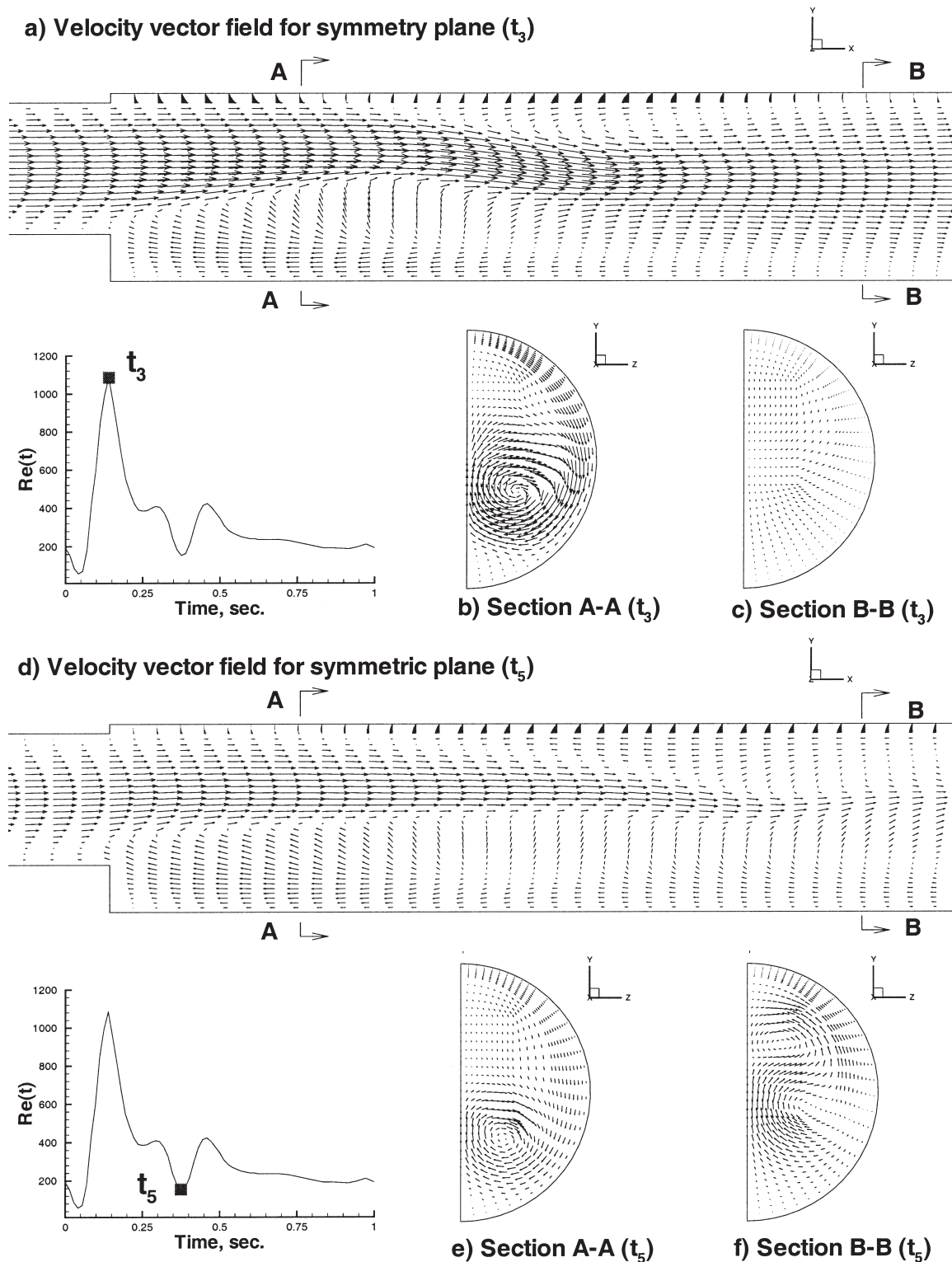
Fig. 4.   Velocity vector fields for asymmetric step expansion geometry at representative time steps.

cally (cf. Fig. 2c and d). The curve for the smooth expansion wall consists of two arcs with the same radius of curvature and the smooth expansion surface for the three-dimensional geometry is interpolated using the curves at the symmetry plane.

Once the flow-field solution is obtained, the equations for the particle trajectory, Eq. (6) with Eqs. (7) and (8) are integrated with the given initial conditions (initial locations and velocity components of the particles) to obtain explicitly the particle location and velocity

a) Velocity vector field for symmetric plane (t₃)

b) Section A-A (t₃)   c) Section B-B (t₃)

d) Velocity vector field for symmetric plane (t₅)

e) Section A-A (t₅)   f) Section B-B (t₅)
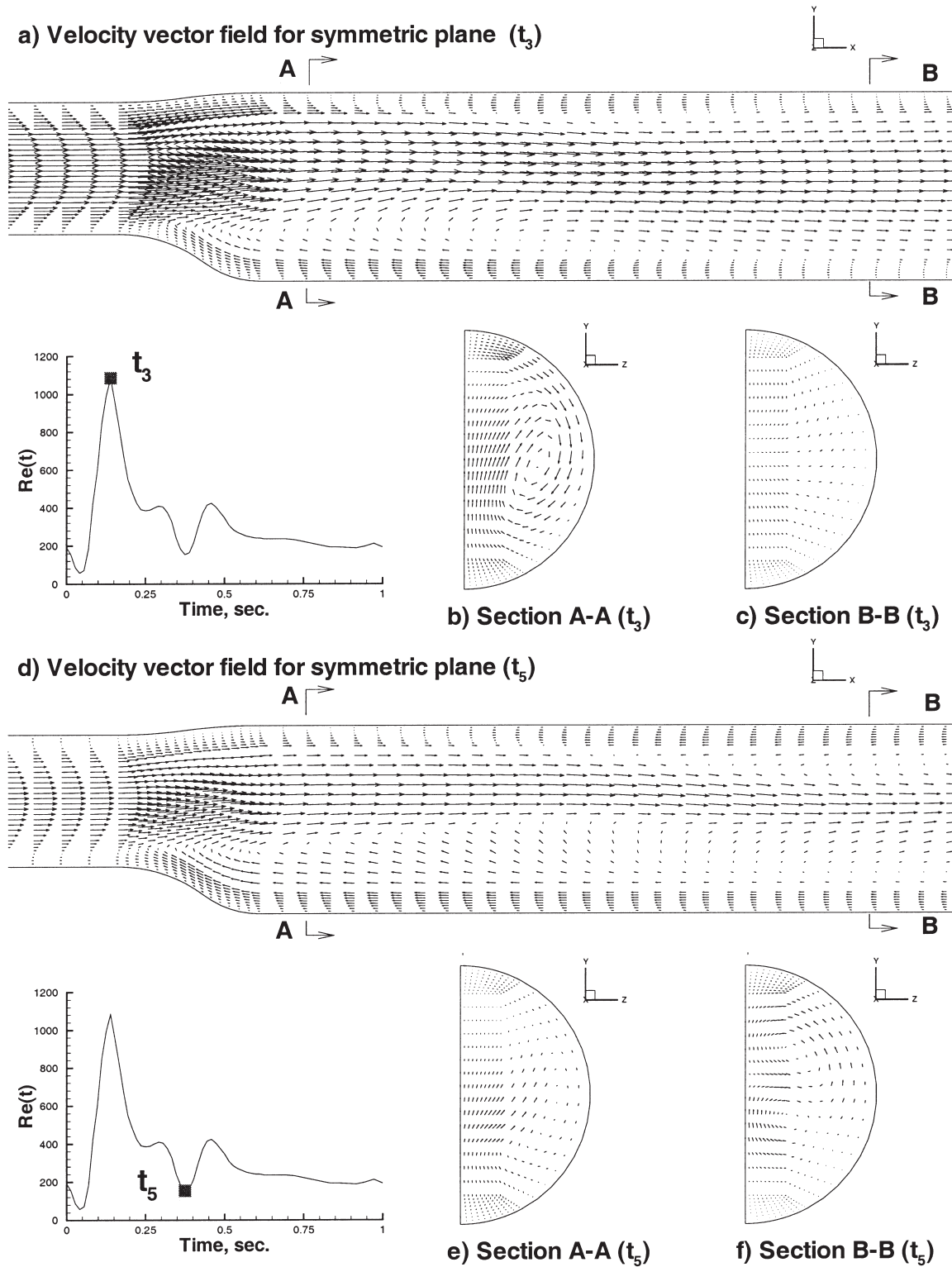
Fig. 5.   Velocity vector fields for asymmetric smooth expansion geometry at representative time steps.

components at any time. This initial value problem is solved numerically with a fourth-order Runge–Kutta routine. The time step for the particle transport is order of 10^{-4} s, which is small enough to remove the time step dependency of a fourth-order Runge–Kutta integration.

3. Results

3.1. Velocity fields

As with most expansion geometries, jet-like flow can be observed especially at time t_3 (cf. Fig. 3a), while

extended recirculation regions exist near the expanding wall at time t_5 for both axisymmetric geometries (cf. Fig. 3a–d). The velocity vector plots provide quite similar flow patterns for both tubular expansions, i.e. recirculation in the vicinity of the expansion wall, strong jet flow around the center line, prolonged recirculation during the decelerating systolic phase, and midstream forward flow throughout the input pulse. The radial extent of the recirculation regions for both axisymmetric expansion cases is equal or larger than the actual expansion height. However, the length of the recirculation region for the step expansion is shorter than that for the smooth expansion.

For the asymmetric expansion cases, the velocity vector plots are very different when compared to the axisymmetric expansion cases. Figs. 4 and 5 represent the velocity vector fields for step and smooth asymmetric expansion geometries, respectively. Special features of three-dimensional asymmetric flow include jet-like undulating, contracting and expanding flow near the center of the tube while the slower moving fluid near the wall recirculates. At peak systole (cf. Figs. 4d–f and 5d–f), strong vortical flow is found in the lower part of the cross section near the expansion (cf. Section A-A). This helical motion decays fast, so it cannot be found downstream at section B-B, about four times of the exit diameter away from the expansion. At the end of systole (cf. Figs. 4d–f and 5d–f), the flow in the center area of the tube is forward, but reverse flow exists near the wall for the entire tube length. As expected, due to the lower Reynolds number inlet condition, forward as well as spiral motions are weaker than those for peak systole.

Although jetting flow may create a high wall shear stress environment upstream and extended recirculation regions with low wall shear stresses downstream from the expansion, it is difficult to make a quantitative distinction in terms of disturbed flow characteristics between the two geometries, i.e., step and smooth expansions. However, it is evident that smooth expansion geometries have weaker disturbed flow features than step expansion geometries.

3.2. Disturbed flow indicators

Fig. 6 shows the time-averaged indicators for two-dimensional axisymmetric step and smooth expansion geometries, which are indicated by solid and dotted lines, respectively. Flow separation occurs at the expansion wall, $x=0$, and flow reattachment, which oscillates in the proximal/distal direction, is observed. Suggested values of the critical WSS are 0.4 dyn/cm^2 for lower WSS and 100 dyn/cm^2 for higher WSS [4]. In the present cases, there is no critical WSS region, i.e., extremely high WSS or low WSS, except near the reattachment point. The WSSG has a maximum near the expansion wall and decreases rapidly to zero downstream. Elevated
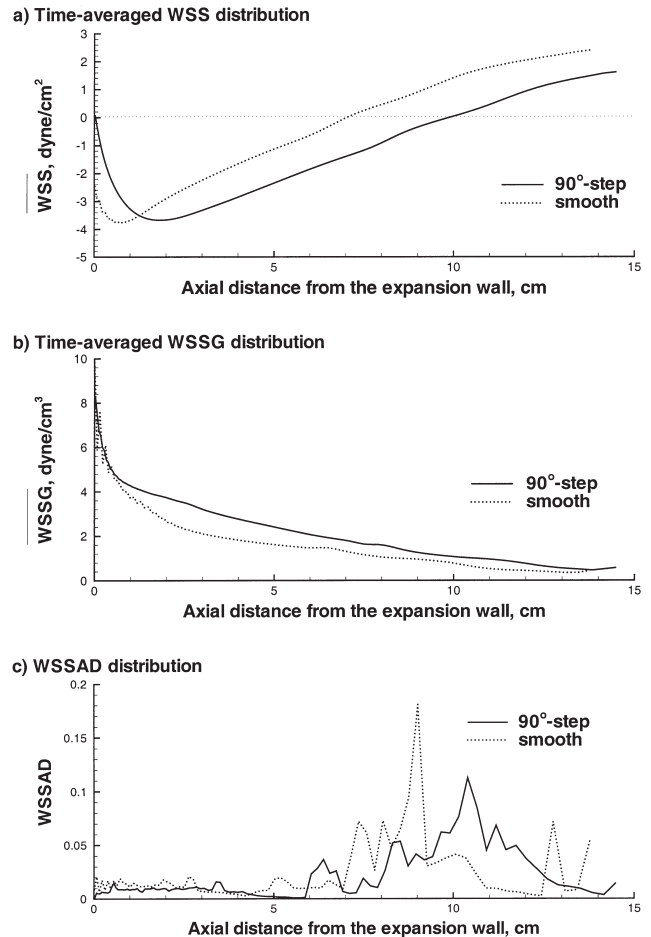
Fig. 6.   Time averaged non-uniform hemodynamic indicator distributions for axisymmetric expansion geometries.

WSSG values are found inside and around the time-averaged reattachment point. The new indicator, WSSAD, has a maximum at the time-averaged reattachment point and elevated values near it. The smooth expansion geometry exhibits for the most part lower values in terms of disturbed flow indicators, which implies a lower probability of an incidence of arterial diseases, as was observed clinically [8].

For three-dimensional asymmetric expansion geometries, non-uniform hemodynamic indicators are shown in Figs. 7 and 8. Lower WSS regions exist near the expansion wall and downstream of the expansion wall, coinciding with flow separation zones (cf. Fig. 7a and b). Flow separation occurs along the lateral wall and helical motion of flow near the wall is observed. A higher WSSG is focally found just near the expansion wall. The WSSAD, which indicates abnormal endothelial cell morphology changes and potential particle deposition, is higher near the expansion wall as well as downstream along the lateral wall. The smooth expansion exhibits more uniform WSS contours than the step expansion; however, very high WSSG-values are found at the expansion wall. Higher WSSAD regions are found near

a) Time-averaged WSS contours
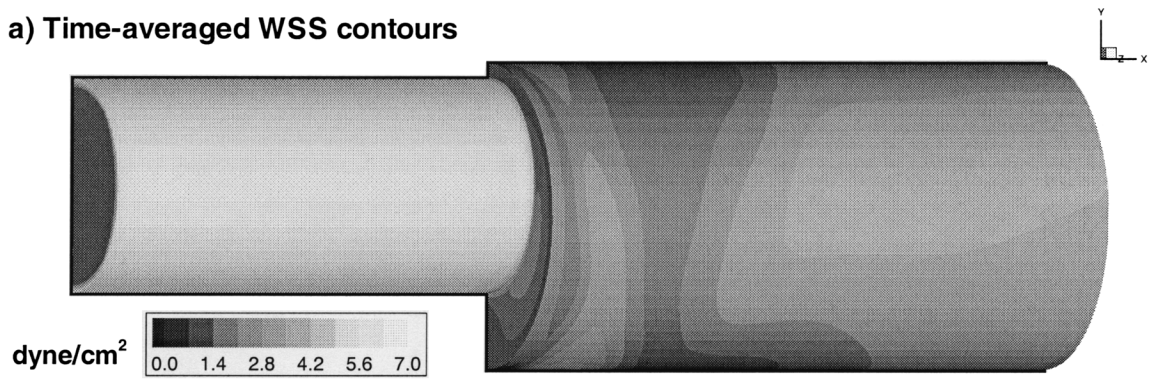
dyne/cm^2

0.0 1.4 2.8 4.2 5.6 7.0

b) Time-averaged WSS vector distribution

c) Time-averaged WSSG contours

dyne/cm^3

0.0 2.0 4.0 6.0 8.0 10.0

d) WSSAD contours

-0.1 0.3 0.7 1.2 1.6 2.0
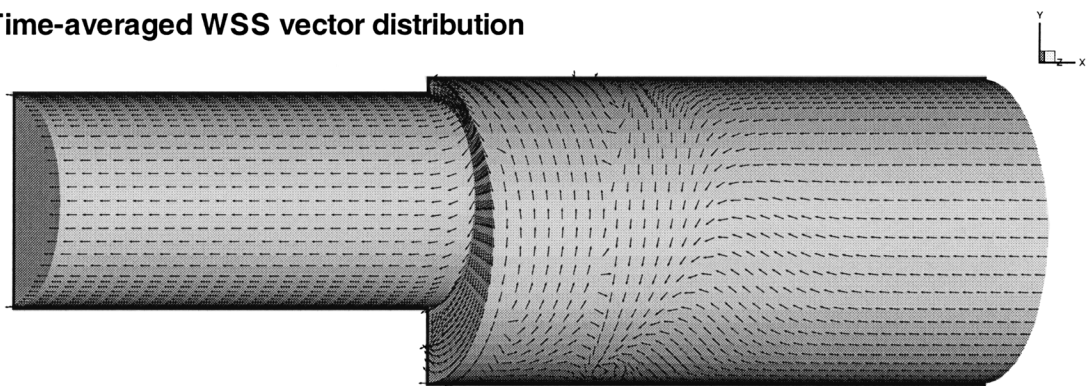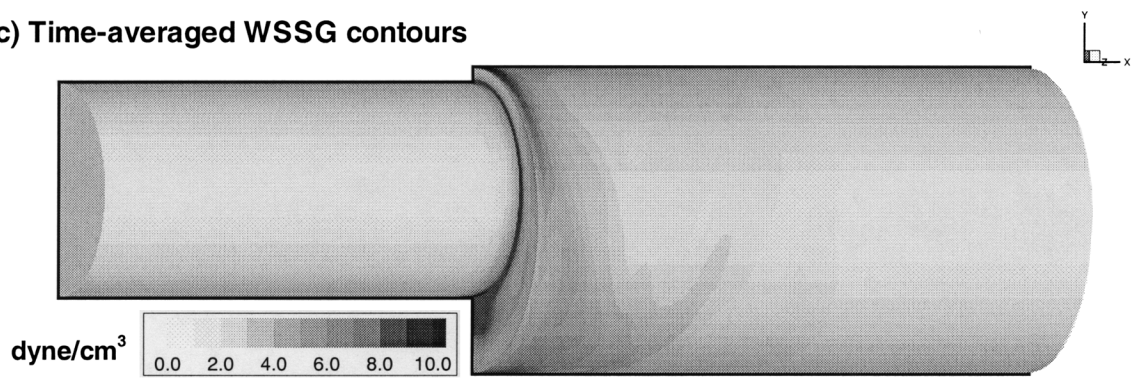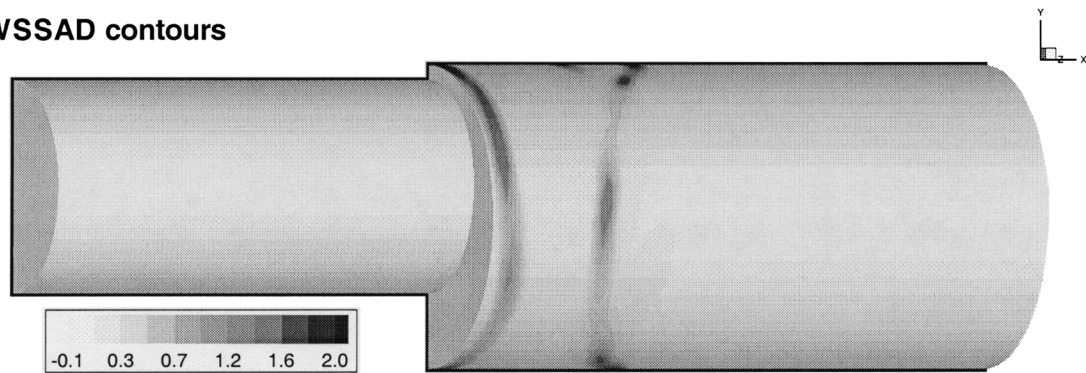
Fig. 7. Time averaged non-uniform hemodynamic indicator distributions for asymmetric step expansion geometry.

a) Time-averaged WSS contours
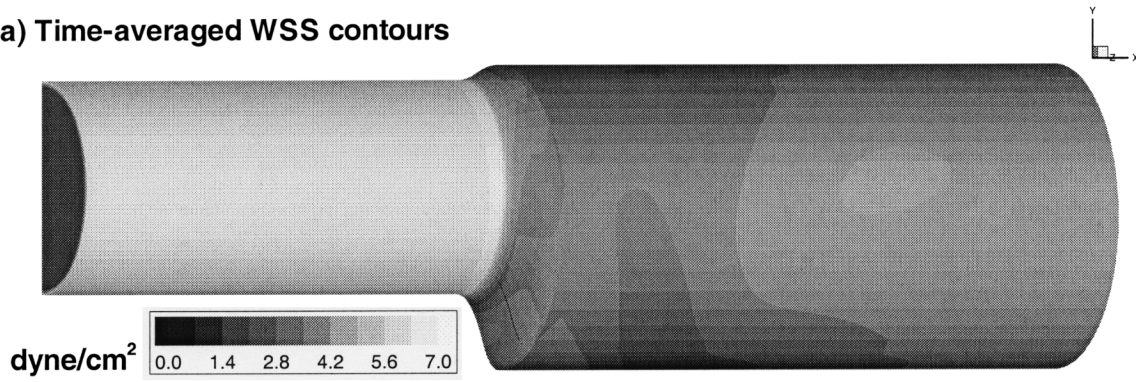
dyne/cm² 0.0 1.4 2.8 4.2 5.6 7.0

b) Time-averaged WSS vector distribution

c) Time-averaged WSSG contours

dyne/cm³ 0.0 2.0 4.0 6.0 8.0 10.0

d) WSSAD

-0.1 0.3 0.7 1.2 1.6 2.0
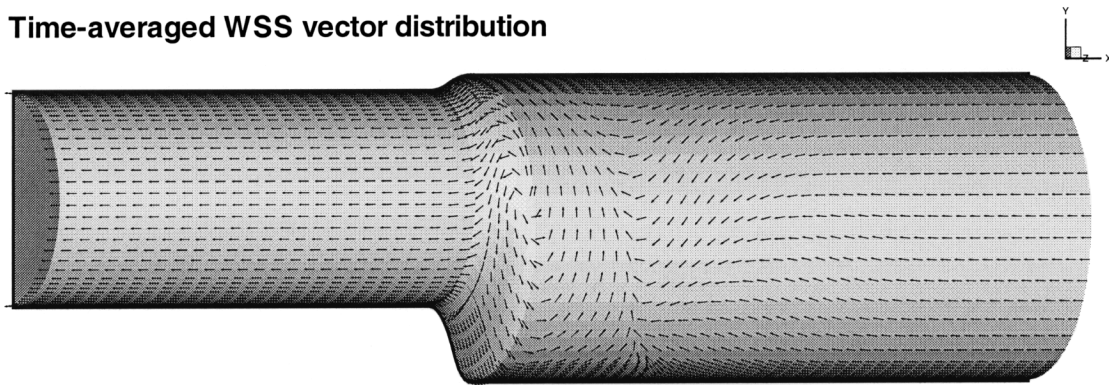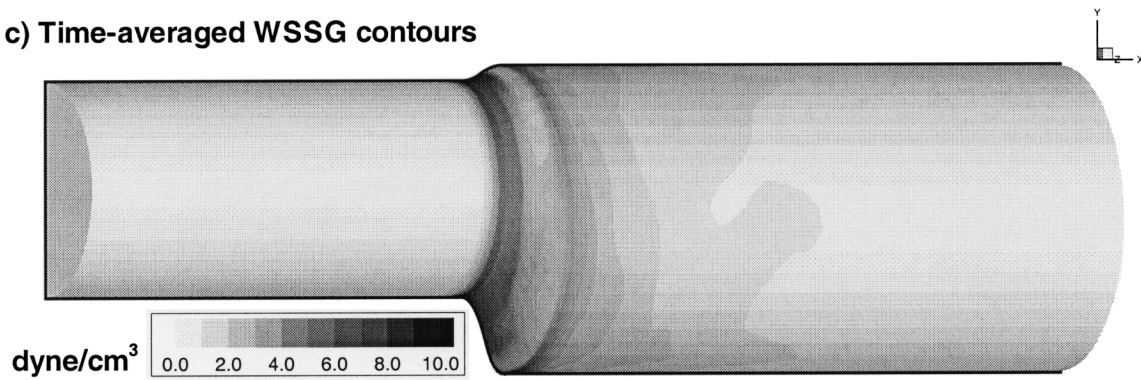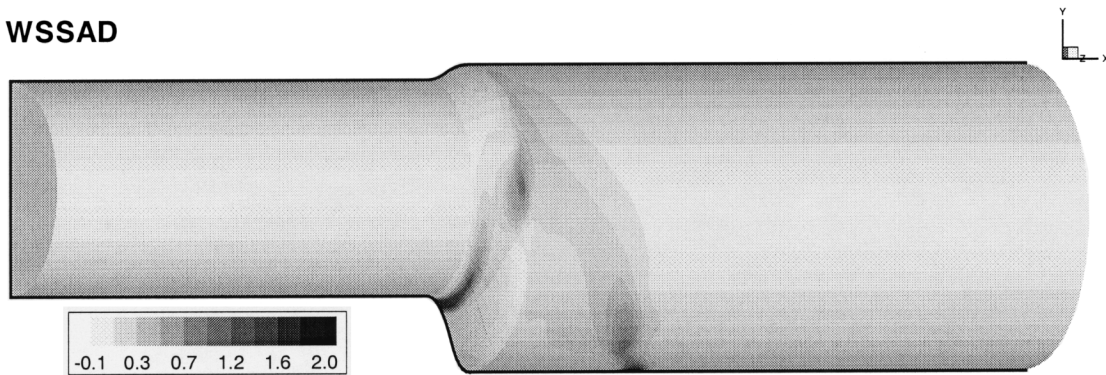
Fig. 8.   Time averaged non-uniform hemodynamic indicator distributions for asymmetric smooth expansion geometry.

the expansion wall and the lateral wall. The trends of disturbed flow indicator distributions for the smooth expansion geometry are similar to those for the step expansion geometry, but the affected area for the smooth expansion geometry is smaller.

3.3. Particle trajectories

To study particle aggregation and deposition, near-wall particle motion is observed, and particle deposition patterns for axisymmetric expansion geometries are compared with WSSAD distributions (cf. Fig. 9). At time $t=t_0$, it is assumed that a large number of particles are uniformly distributed inside the flow field with initial radial locations of particles 10 μm away from the wall. 200 uniformly distributed particles are seeded for axisymmetric expansion geometries. Particles are deposited when the distance of the particle center from the wall is less than or equal to 7 μm. The steady-state result shows the maxima of particle deposition near the time-averaged reattachment point (cf. Fig. 9a) which coincides with the locations of WSSAD peaks (cf. Fig. 9b). The results for axisymmetric particle deposition distribution are similar to those experimentally measured data from Karino et al. [16] and Pritchard et al. [18], which is summarized in Hyun [35].

Particle transport simulations were also performed for asymmetric geometries (cf. Figs. 10 and 11) and compared to WSSAD surface contours. At time $t=t_0$, a large number of particles (3000 particles) are evenly distributed throughout the flow field as shown in Figs. 10a or 11a. The initial distance from the wall in this case is 100 μm. As time elapses, some particles deposit on the wall, and others are convected downstream (cf. Figs. 10b and 11b). Particle deposition and accumulation occur along the lateral wall, where flow separation is observed and particle residence time is prolonged (cf. Figs. 10c and 11c). The high particle deposition region correlates well with elevated WSSAD contour areas (cf. Figs. 10d and 11d).

4. Discussion

Over the last two decades it has been well documented that non-uniform hemodynamics, i.e. areas of "disturbed flow", play a significant role in the onset and progression of abnormal biological events in large arteries with complex geometries, i.e. bends, bifurcations, branches as well as sudden expansions or partial occlusions. A carotid endarterectomy (CEA) producing a step in the common carotid artery is the first source of flow disturbance in a reconstructed carotid artery, and thrombi formation and recurrent arterial disease are generally localized over the expansion surfaces of the adjacent endarterectomized wall. This upstream source of disturbed flow should be reduced to minimize downstream disturbances in the bifurcation or in reconstructed carotid arteries.

In this study, the transient flow structures and particle transport in the vicinity of axisymmetric and asymmetric expansions are simulated and possible links between disturbed flow indicators with particle transport and postoperative complications in endarterectomized common carotid artery are analyzed.

In general, recirculation zones behind the expansion, zero-flow areas in the expansion corner, negative radial pressure gradients, and positive normal velocities toward the wall near reattachment points are found in those geometries. For asymmetric geometries, no closed zones of recirculating flow exist, but helical flow behind the expansions is observed. The smooth expansions are better than 90°-step expansions because near-zero WSS areas and extended disturbed flow patterns are largely avoided. However, the exact form of gradual expansion, i.e. slanted, smooth 2nd-order, smooth 3rd-order, etc., was immaterial as shown by Hyun [35]. In general, all non-uniform hemodynamic indicators spike at the expansion edge and along the expansion wall for both expansion geometries.

a) Particle deposition patterns

b) Distribution of Wall shear stress angle deviation function
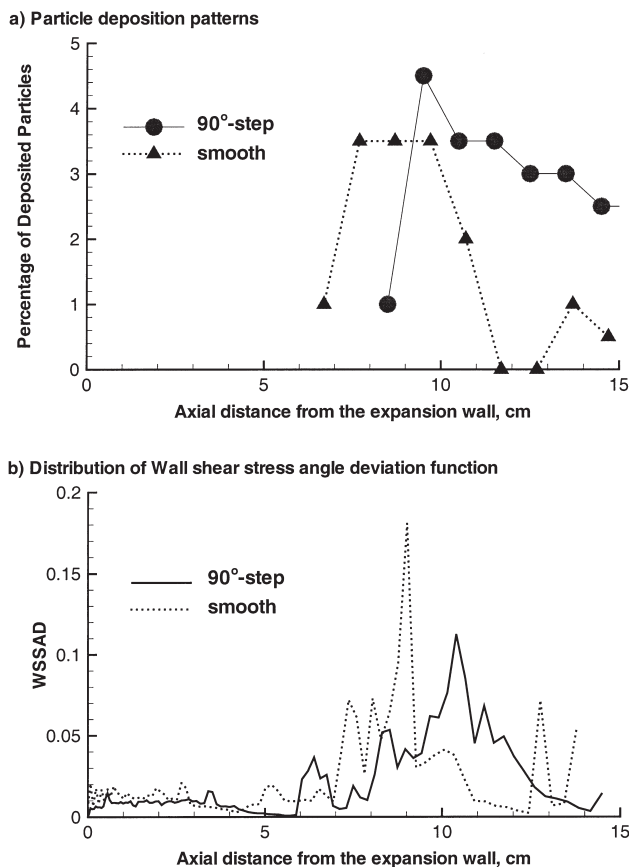
Fig. 9. Particle deposition patterns compared with wall shear stress angle deviation distribution.
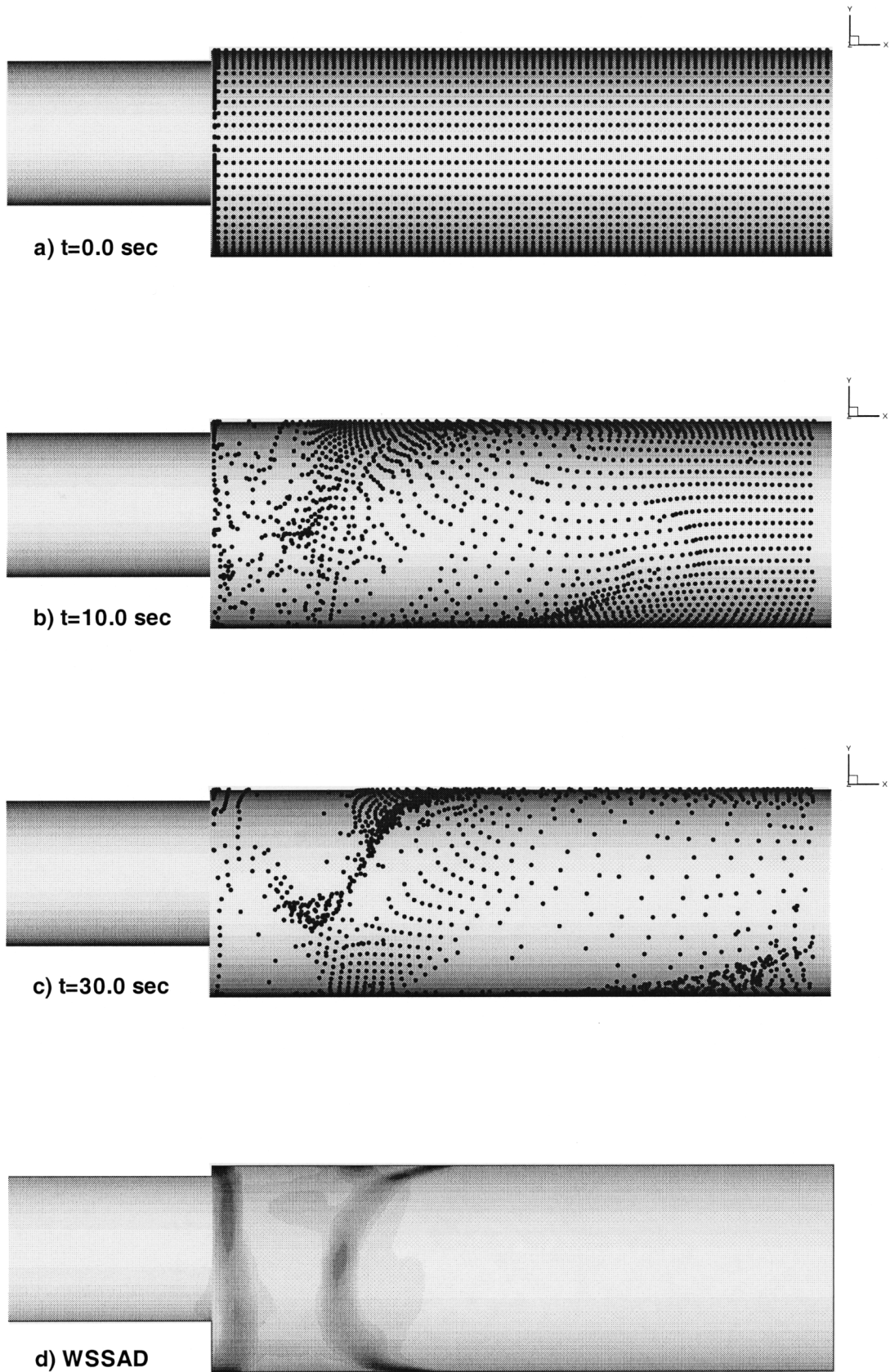
Fig. 10.   Transient particle deposition and accumulation for asymmetric step expansion geometry compared with wall shear stress angle deviation contour plot.
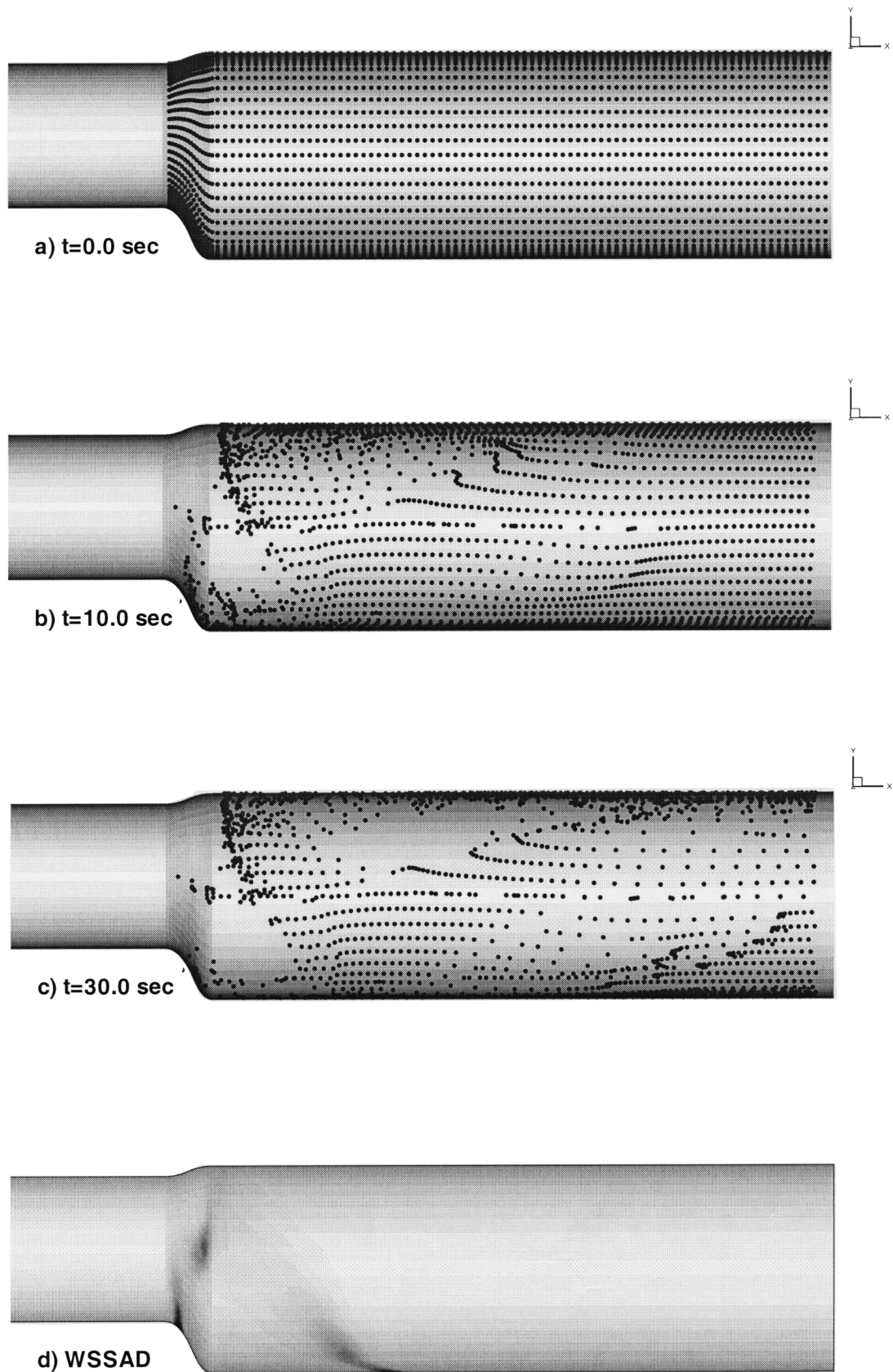
Fig. 11. Transient particle deposition and accumulation for asymmetric smooth expansion geometry compared with wall shear stress angle deviation contour plot.

The particle behavior shows that the region near the expansion wall is a susceptible place for extended particle entrainment, aggregation, and possibly for particle deposition where particle residence time is prolonged. The smooth expansion shows less deposition of particles. For the smooth expansion geometry, the particle deposition distribution shows that most of the particles are entrained by the main stream and convected downstream and no permanent stasis or deposition is observed. The particle transport simulation results for three-dimensional expansion geometries are different from those for 2-D axisymmetric expansion geometries.

The wall shear stress angle deviation (WSSAD), which is a new non-uniform hemodynamic indicator representing abnormal endothelial cell morphology and particle transport near the wall, correlates well with susceptible sites of near-wall particle accumulation and wall deposition. Hence, high WSSAD contour regions indicate areas with abnormal changes in endothelial cell morphology, which is characterized by polygonal cell shapes with larger intercellular gaps. In addition, as in the region of stagnant (or reattachment point) flow, normal velocity components toward the wall and reverse pressure gradients influence particle accumulation and deposition. High WSSAD regions can be expected in atherosclerotic lesion-prone regions and in areas of thrombotic particle aggregation and wall deposition.

Generally, low WSS and high WSSG regions are recognized as susceptible sites for arterial diseases. Thus, it is interesting to note that high WSSAD regions covers low WSS as well as high WSSG locations.

Acknowledgements

References

[1] Lei M, Archie JP, Kleinstreuer C. Computational design of a bypass graft that minimize wall shear stress gradients in the region of the distal anastomosis. Journal of Vascular Surgery 1997;25:637–46.

[2] He X, Ku D. Pulsatile flow in the human left coronary artery bifurcation: average conditions. ASME Journal of Biomechanical Engineering 1996;118:74–82.

[3] Chandran KB, Kim Y-H. Mechanical aspects of vascular graft-host artery anastomoses. IEEE Engineering in Medicine and Biology 1994;August/September:517–24.

[4] Giddens DP, Zarins CK, Glagov S. The role of fluid mechanics in the localization and detection of atherosclerosis. Journal of Biomechanical Engineering 1993;115:14–23.

[5] Nerem RM. Vascular fluid mechanics, the arterial wall, and atherosclerosis. ASME Journal of Biomechanical Engineering 1992;114:274–82.

[6] Badimon L, Badimon JJ, Turitto VT, Fuster V. Role of von Willebrand factor in mediating platelet-vessel wall interaction at low shear rate; the importance of perfusion conditions. Blood 1989;73(4):961–7.

[7] Goldsmith HL, Turitto VT. Rheological aspects of thrombosis and haemostasis: basic principles and applications. Trombo Haemost 1986;55:415–35.

[8] Kleinstreuer C, Lei M, Archie JP Jr. Hemodynamics simulations and optimal computer-aided designs of branching blood vessels. In: Leondes C, editor. Biomechanic systems techniques and applications. New York: Gordon and Breach, 2000.

[9] Archie JP. The endarterectomy produced common carotid artery step: a harbinger of early emboli and late restenosis. Journal of Vascular Surgery 1996;23(5):932–9.

[10] Okano M, Yoshida Y. Endothelial cell morphometry of atherosclerotic lesions and flow profiles at aortic bifurcations in cholesterol fed rabbits. Journal of Biomechanical Engineering 1992;114:301–8.

[11] Nerem RM, Levesque MJ, Cornhill JF J.F.. Vascular endothelial morphology as an indicator of the pattern of blood flow. Journal of Biomechanical Engineering 1981;103:172–6.

[12] Shettigar UR, Dropmann M, Christian PE, Kolff WJ. Residence time distributions in artificial ventricles. Transaction of the American Society of Artificial Internal Organs 1989;XXXV:708–12.

[13] Back MR, Cho YI, Crawford DW, Back LH. Fluid particle motion and lagrangian velocities for pulsatile flow through a femoral artery branch model. Journal of Biomechanical Engineering 1987;109:94–101.

[14] Karino T, Goldsmith L. Particle flow behavior in models of branching vessels: II. Effects of branching angle and diameter ratio on flow patterns. Biorhoelogy 1985;22:87–104.

[15] Karino T, Goldsmith HL. Flow behavior of blood cells and rigid spheres in an annular vortex, Philosophical Transactions of the Royal Society of London, series B. Biological Sciences 1977;279:413–45.

[16] Karino T, Herman HM, Goldsmith L. Particle flow behavior in models of branching vessels: I. Vortices in 90° T-junctions. Biorhoelogy 1979;16:231–48.

[17] Blackshear PL, Forstrom RJ, Lorberbaum M, Gott VL, Sovilj R. A role of flow separation and recirculation in thrombi formation on prosthetic surfaces, AIAA 9th Aerospace Sciences Meeting, paper 71-103, 1971.

[18] Pritchard WF, Davis PF, Derafsi Z, Polacek DC, Tsao R, Dull RO, Jones SA, Giddens DP. Effects of wall shear stress and fluid recirculation on the localization of circulating monocytes in a three-dimensional flow model. Journal of Biomechanics 1995;28(12):1459–69.

[19] Buchanan JR Jr., Kleinstreuer C. Simulation of particle-hemodynamics in a partially occluded artery segment with implications to the initiation of microemboli and secondary stenoses. Journal of Biomechanical Engineering 1998;120:446–54.

[20] Kunov MJ, Steinman DA, Ethier CR. Particle volumetric residence time calculations in arterial geometries. Journal of Biomechanical Engineering 1996;118:158–64.

[21] Srivastava VP. Particle-fluid suspension model of blood flow through stenotic vessels with applications. International Journal of Bio-Medical Computing 1995;38:141–54.

[22] Uijttewaal SJW, Nijhof EJ, Heethaar RM. Lateral migration of blood cells and microspheres in two-dimensional Poiseulle flow: A laser-doppler study. Journal of Biomechanics 1994;27:35–42.

[23] Nazemi M, Kleinstreuer C. Analysis of particle trajectories in aortic artery bifurcations with stenosis. Journal of Biomechanical Engineering 1989;111:311–5.

[24] Kleinstreuer C, Hyun S. Computer simulation of dilute suspension flows in branching blood vessels. In: Martonen TB, editor.

Computer modeling and fluid dynamics of biological systems. Amshurst, Southampton, UK: WIT Press, 2000.

[25] Bharadvaj BK, Mabon RF, Giddens DP. Steady flow in a model of the human carotid bifurcation. Part I — flow visualization. Journal of Biomechanics 1982;15(5):349–62.

[26] Hyun S, Kleinstreuer C, Archie JP. Transient hemodynamics analyses in sudden expansions with implications to thrombosis, embolization and restenosis. In: Gerbsch R, Elger DF, editors. FED SM97 Conference Proceedings. New York: ASME, 1997.

[27] Kleinstreuer C. Engineering fluid dynamics — an interdisciplinary systems approach. New York: Cambridge University Press, 1997.

[28] Macosko RA. Rheology: principles, measurements, and applications. New York: VCH Publications, 1994.

[29] Merrill EW. Rheology of blood. Physiological Reviews 1969;49(4):863–88.

[30] Bluestein D, Niu L, Schoephoerster RT, Dewanjee MK. Fluid mechanics of arterial stenosis: Relationship to the development of mural thrombus. Annals of biomechanical Engineering 1997;25:344–56.

[31] Lei M. Computational fluid dynamics analyses and optimal design of bifurcating blood vessels. Ph. D. Thesis, MAE Department, North Carolina State University, 1995.

[32] AEA Technology. CFX-F3D users manuals for Vers. 4.1. Pittsburgh: AEA Technology, 1996.

[33] Patankar SV. Numerical heat transfer and fluid flow. Washington: Hemisphere Publishing Co, 1980.

[34] Lonsdale RD. An algebraic multigrid solver for the Navier-Stokes equations on unstructured meshes. International Journal of Numerical Methods for Heat and Fluid Flow 1993;3:3–14.

[35] Hyun S. Transient particle-hemodynamics simulations in three-dimensional carotid artery bifurcations. Ph. D. Thesis, Raleigh, NC, Dept., of MAE, North Carolina State University, 1998.